An increase in the ^{12}C + ^{12}C fusion rate from resonances at astrophysical energies

A. Tumino[1,2]*, C. Spitaleri[2,3], M. La Cognata[2], S. Cherubini[2,3], G. L. Guardo[2,4], M. Gulino[1,2], S. Hayakawa[2,5], I. Indelicato[2], L. Lamia[2,3], H. Petrascu[4], R. G. Pizzone[2], S. M. R. Puglia[2], G. G. Rapisarda[2], S. Romano[2,3], M. L. Sergi[2], R. Spartá[2] & L. Trache[4]

Carbon burning powers scenarios that influence the fate of stars, such as the late evolutionary stages of massive stars[1] (exceeding eight solar masses) and superbursts from accreting neutron stars[2,3]. It proceeds through the ^{12}C + ^{12}C fusion reactions that produce an alpha particle and neon-20 or a proton and sodium-23—that is, ^{12}C(^{12}C, α)^{20}Ne and ^{12}C(^{12}C, p)^{23}Na—at temperatures greater than 0.4×10^9 kelvin, corresponding to astrophysical energies exceeding a megaelectronvolt, at which such nuclear reactions are more likely to occur in stars. The cross-sections[4] for those carbon fusion reactions (probabilities that are required to calculate the rate of the reactions) have hitherto not been measured at the Gamow peaks[4] below 2 megaelectronvolts because of exponential suppression arising from the Coulomb barrier. The reference rate[5] at temperatures below 1.2×10^9 kelvin relies on extrapolations that ignore the effects of possible low-lying resonances. Here we report the measurement of the ^{12}C(^{12}C, $\alpha_{0,1}$)^{20}Ne and ^{12}C(^{12}C, $p_{0,1}$)^{23}Na reaction rates (where the subscripts 0 and 1 stand for the ground and first excited states of ^{20}Ne and ^{23}Na, respectively) at centre-of-mass energies from 2.7 to 0.8 megaelectronvolts using the Trojan Horse method[6,7] and the deuteron in ^{14}N. The cross-sections deduced exhibit several resonances that are responsible for very large increases of the reaction rate at relevant temperatures. In particular, around 5×10^8 kelvin, the reaction rate is boosted to more than 25 times larger than the reference value[5]. This finding may have implications such as lowering the temperatures and densities[8] required for the ignition of carbon burning in massive stars and decreasing the superburst ignition depth in accreting neutron stars to reconcile observations with theoretical models[3].

We measured the ^{12}C(^{14}N, α^{20}Ne)^{2}H and ^{12}C(^{14}N, p^{23}Na)^{2}H three-body processes in the quasi-free kinematic regime using the Trojan Horse Method (THM). The THM is an indirect technique with which to measure low-energy nuclear reactions unhindered by the Coulomb barrier and free of electron screening. The experimental and analysis procedures are detailed in Methods sections 'THM basic features', 'One-level many-channel THM formalism', 'Experimental setup and channel selection' and 'Deuteron momentum distribution'. The experiment was performed at INFN, Laboratori Nazionali del Sud, Italy. A 30-MeV ^{14}N beam accelerated by the MP Tandem accelerator was delivered onto a carbon target. The detection setup consisted of two silicon telescopes, devoted to the detection of α–d and p–d coincidences. The occurrence and the dominance of the quasi-free mechanism[5] was indicated by the agreement between the shapes of the experimental and the theoretical d momentum distributions (Extended Data Fig. 1).

The THM experimental yields projected onto the ^{12}C–^{12}C relative energy variable, the centre-of-mass energy E_{cm}, are shown as black dots in Fig. 1a (^{20}Ne + α_0), Fig. 1b (^{20}Ne + α_1), Fig. 1c (^{23}Na + p_0) and Fig. 1d (^{23}Na + p_1). A smooth four-body background due to ^{16}O + α + α + d was subtracted from the THM yields for the ^{20}Ne + $\alpha_{0,1}$ channels. Error bars display the statistical errors and account for background subtraction uncertainty, when applicable, combined in quadrature.

A modified one-level many-channel R-matrix analysis was carried out including the excited states of the ^{24}Mg nucleus reported in Extended Data Table 1[9–13]. The fraction of the total fusion yield from α and p channels[14,15] other than $\alpha_{0,1}$ and $p_{0,1}$ was neglected with estimated errors at $E_{cm} < 2$ MeV lower than 1% and 2% for the α and p channels, respectively (see Methods section 'Modified R-matrix analysis').

The results are shown in Fig. 1a–d as red lines and with light-red shading indicating the uncertainties on the resonance parameters, including correlations. Agreement with experimental data is fair and confirmed by the reduced χ^2 (that is, $\widetilde{\chi}^2$) values of 0.73 for ^{20}Ne + α_0, 1.06 for ^{20}Ne + α_1, 0.54 for ^{23}Na + p_0 and 1.34 for ^{23}Na + p_1. The resonance structure observed in the excitation functions is consistent with ^{24}Mg level energies reported in the literature, with some tendency for the even-J states to be clustered[11] at about 1.5 MeV. The THM-reduced widths thus entered a standard R-matrix code[16] and the $S(E)$ factors (see Methods section 'Astrophysical $S(E)$ factor') for the four reaction channels were determined.

The results are shown in Fig. 2a (^{20}Ne + α_0), Fig. 2b (^{20}Ne + α_1), Fig. 2c (^{23}Na + p_0) and Fig. 2d (^{23}Na + p_1), in terms of the modified $S(E)$ factor[15,17], $S(E)$*, (see Methods section 'Astrophysical $S(E)$ factor'). The black line and grey shading in each panel represent the best-fit curve and the range defined by the total uncertainties, respectively. The grey shading is the result of R-matrix calculations with lower and upper values of the resonance parameters provided by their errors after being combined with the normalization one. Excursions from the midline range from 11% to 20%.

The resonant structures are superimposed onto a flat nonresonant background[15] of 0.4×10^{16} MeV b. Unitarity of the S matrix is guaranteed within the experimental uncertainties. Normalization to direct data was done in the E_{cm} window 2.50–2.63 MeV of the ^{20}Ne + α_1 channel, where a sharp resonance corresponding to the 16.5-MeV level[9] of ^{24}Mg appears and available data[15,18–20] in this region are the most accurate of those overlapping with THM data. By scaling to the resonance by means of a weighted normalization, the resulting normalization error is 5%, shown as grey shading in Fig. 2a–d, combined in quadrature with errors on the resonance parameters.
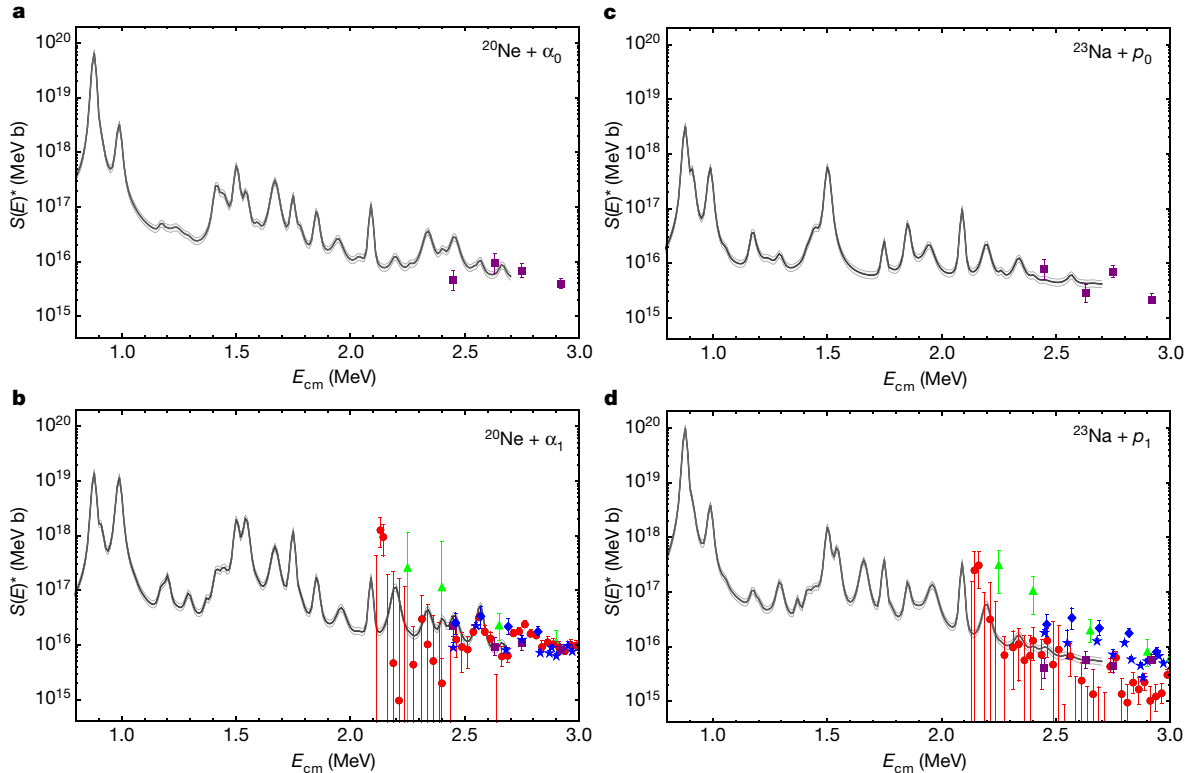
Existing direct data below $E_{cm} = 3$ MeV are shown as red filled circles[15], purple filled squares[18], blue filled diamonds[19], blue filled stars[20] and green filled triangles[21] in Fig. 2. Their low-energy limit is mostly fixed by the background due to hydrogen contamination in the targets[18–21] and the higher $S(E)$ values for the p_1 channel in some of them[19–21] were attributed to Coulomb excitation of ^{23}Na contamination in the targets or collimators[15,20]. Disregarding these cases, agreement between THM results and direct data are apparent within the experimental errors, except for the direct low-energy limit around 2.14 MeV, where THM data do not confirm the claim of a strong resonance; instead, there is a nearby resonance at 2.095 MeV, about one order of magnitude less intense in the ^{20}Ne + α_1 channel (see Fig. 2b) and with similar intensity in the ^{23}Na + p_1 one (see Fig. 2d). The present

[1]Facoltá di Ingegneria e Architettura, Universitá degli Studi di Enna "Kore", Enna, Italy. [2]INFN, Laboratori Nazionali del Sud, Catania, Italy. [3]Dipartimento di Fisica e Astronomia, Universitá degli Studi di Catania, Catania, Italy. [4]Horia Hulubei National Institute for R&D in Physics and Nuclear Engineering, Bucharest-Magurele, Romania. [5]Center for Nuclear Studies, The University of Tokyo, Tokyo, Japan. *e-mail: tumino@lns.infn.it
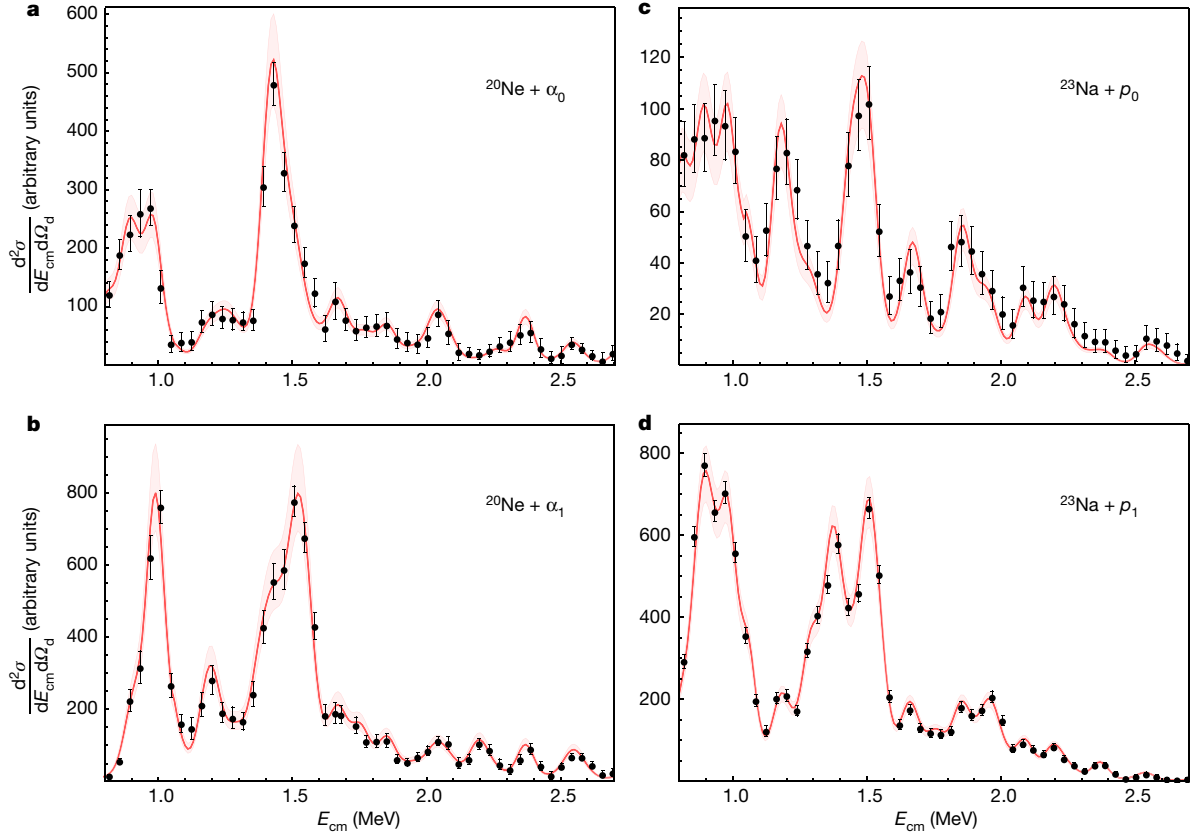
Fig. 1 | Excitation functions from THM experimental yields. The quasi-free cross-section for the four channels ^{20}Ne + α_0 (**a**), ^{20}Ne + α_1 (**b**), ^{23}Na + p_0 (**c**) and ^{23}Na + p_1 (**d**) is projected onto the E_{cm} variable (black dots). Error bars denote $\pm 1\sigma$ uncertainties and account for background subtraction (combined in quadrature). Red lines and light-red shading represent the results of the modified R-matrix fits and the related uncertainties, respectively.

Fig. 2 | ^{12}C + ^{12}C astrophysical $S(E)*$ factors. The THM $S(E)*$ factors for the four channels ^{20}Ne + α_0 (**a**), ^{20}Ne + α_1 (**b**), ^{23}Na + p_0 (**c**) and ^{23}Na + p_1 (**d**) are shown as black lines. The available direct data in the E_{cm} range investigated are reported as red filled circles[15], purple filled squares[18], blue filled diamonds[19], blue filled stars[20] and green filled triangles[21]. The upper and lower grey lines mark the range arising from $\pm 1\sigma$ uncertainties on resonance parameters plus the normalization to direct data in the ^{20}Ne + α_1 channel at $E_{cm} = 2.50$–2.63 MeV.

result is in agreement with spectroscopy studies[9,22] that report a dip at 2.14 MeV and no particularly strong α state at around 2.1 MeV. Further agreement is found with unpublished experimental data down to $E_{cm} = 2.15$ MeV for the $^{12}C(^{12}C, p_{0,1})^{23}N$ reactions[23]. Our result is also consistent within experimental errors with the total $S(E)^*$ from a recent experiment at higher energies[24], which was calculated at the overlapping $E_{cm} = 2.68 \pm 0.08$ MeV.

The reaction rates for the four processes were calculated from the THM $S(E)^*$ factors using the standard formula[4] and summed to obtain the total $^{12}C + ^{12}C$ reaction rate. Its numerical values are given in Extended Data Table 2 (see Methods section 'Numerical values of the $^{12}C + ^{12}C$ reaction rate'). We recommend an analytical expression for the reaction rate and for its upper and lower limits, based on the same formulae as reported in the REACLIB library[25]. This expression is valid in the temperature range 0.1 GK $\leq T \leq$ 3 GK with an accuracy better than 0.7% ($\tilde{\chi}^2 = 0.1$), which refers to the maximum difference between the analytical function and the centroids of the experimental points. This is given by:

$$N_A \langle \sigma v \rangle = \sum_{i=1}^{3} f_i = \sum_{i=1}^{3} \exp[a_{i1} + a_{i2}T^{-1} + a_{i3}T^{-1/3} \\ + a_{i4}T^{1/3} + a_{i5}T + a_{i6}T^{5/3} + a_{i7}\ln(T)] \tag{1}$$

Parameters a_{ij} with $1 < i < 3$ and $1 < j < 7$ are given in Table 1, with subscripts 'u' and 'l' for the upper and lower limits. They result from a fit performed using the NUCASTRODATA toolkit (http://www.nucastrodata.org/).

The total THM reaction rate was divided by the reference rate[5]. The resulting ratio is shown in Fig. 3. The black line represents the rate from the present work, with the grey shading defining the region fixed by the total uncertainty (Methods section 'Numerical values of the $^{12}C + ^{12}C$ reaction rate'), whereas the red line refers to the reference rate[5].

The light-blue shading shows the temperature range relevant for superbursts (about 0.4–0.5 GK), the light-red shading highlights typical temperatures for hydrostatic carbon burning in massive stars (about 0.6–1.0 GK in the core and up to 1.2 GK in the shell, depending on the stellar mass), whereas the light-green shading marks the temperatures of explosive carbon burning (about 1.8–2.5 GK). As shown in Fig. 3, the reaction rate changes below 2 GK with an increase with respect to the reference non-resonant one[5] from a factor of 1.18 at 1.2 GK (***$P < 0.001$) to a factor of more than 25 at 0.5 GK (****$P < 0.00001$). The latter increase, mainly due to the resonances around $E_{cm} = 1.5$ MeV, supports the conjectured fiducial value[3] required to reduce the theoretical superburst ignition depths in accreting neutron stars by a factor of 2 for a range of realistic parameters and core neutrino emissivities. This change matches the observationally inferred ignition depths and can be translated into an ignition temperature below 0.5 GK, compatible with the calculated crust temperature. In other words, carbon burning can trigger superbursts. A similar decrease in temperature is obtained by using the crust Urca shell neutrino emissivities[26], recently invoked to explain the cooling of the outer neutron star crust, while thermally decoupling the surface layers from the deeper crust. Under this hypothesis, a revision of current superburst models and predicted light curves is required and our finding could represent the missing heat source in the standard carbon ignition scenario.
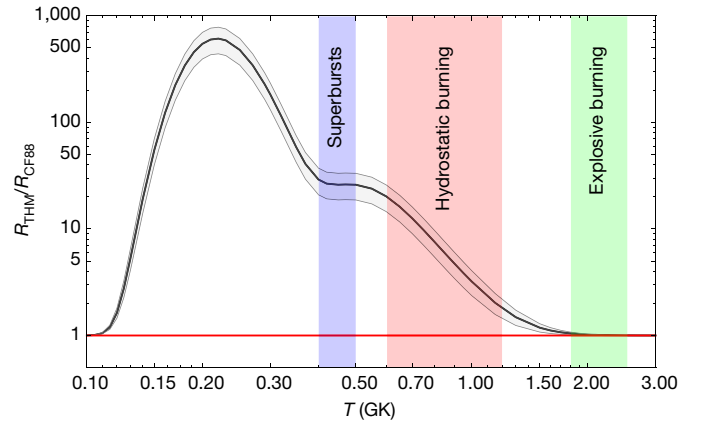
Fig. 3 | $^{12}C + ^{12}C$ reaction rate ratio. Ratio between the total THM $^{12}C + ^{12}C$ reaction rate (black line) and the reference one[4] (red line). The grey shading defines the region spanned owing to the $\pm 1\sigma$ uncertainties. The coloured shading marks typical temperature regions for carbon burning in different scenarios: light blue for superbursts from accreting neutron stars, light red for hydrostatic carbon burning in massive stars and light green for explosive carbon burning; comparison with the red line (non-resonant assumption) gives ***$P < 0.001$ in the region of hydrostatic burning and ****$P < 0.00001$ at superburst temperatures.

In the hydrostatic carbon burning regime, the present rate change will lower the temperatures and densities at which ^{12}C ignites in massive post-main-sequence stars. We make use of stellar modelling[8] for core carbon burning of a star of 25 solar masses to determine that the ignition temperature and density would decrease to 10% and 30% respectively. This would reduce the neutrino losses, thus causing the carbon burning stage to occur for a lifetime (of the carbon burning phase) longer by up to a factor of 70. The new rate would also affect abundances of species that are the main fuel for subsequent evolutionary phases. However, such abundances are influenced also by the ratio of the α to p yields if it deviates from unity. From the present experiment, the average value of this ratio is around 2. In particular, at 0.8 GK this ratio is 1.6 ± 0.4, and it becomes 2.2 ± 0.6 at 2 GK. The $^{12}C + ^{12}C$ rate is also the most important nuclear physics input governing the minimum stellar mass M_{up} required for hydrostatic carbon burning to occur. M_{up} is fundamental to our understanding, for instance, of the evolution of supernova progenitors and the white dwarf luminosity functions. From the present result, we consider that the present value of M_{up} will not be strongly affected, in contrast to what has been predicted[27,28] when assuming a much larger increase (up to nine orders of magnitude) in the reaction rate, but it is worth noticing that stellar models are also very sensitive to small changes of this parameter. However, a sound evaluation of M_{up} requires a better understanding of the ratio of the initial mass to the final core mass.

Below 0.4 GK the rate experiences a huge increase by up to a factor of 800 owing to the lowest-energy resonances occurring around $E_{cm} = 1$ MeV. It has been conjectured that the existence of such low-energy resonances might shift the ignition curve of type Ia supernovae to lower central densities[3]. This should be assessed for the various progenitor scenarios. Much additional work is needed

Table 1 | Coefficients of the analytical function of the $^{12}C + ^{12}C$ reaction rate using equation (1)

a_{ij}	f_1	f_2	f_3	f_{1u}	f_{2u}	f_{3u}	f_{1l}	f_{2l}	f_{3l}
a_{i1}	1.22657×10^2	9.03221×10^1	2.28039×10^2	1.22687×10^2	9.03982×10^1	2.28056×10^2	3.21570×10^2	6.08741×10^2	3.14593×10^3
a_{i2}	0.557112	-8.35888	-1.16039×10^1	0.557664	-8.35720	-1.15681×10^1	-0.815182	-1.42976×10^1	-2.26169×10^1
a_{i3}	-905657×10^1	-6.17552×10^1	-2.40364×10^2	-9.05616×10^1	-6.17282×10^1	-2.40343×10^2	3.17671×10^1	3.43845×10^2	1.36110×10^3
a_{i4}	-6.83561×10^1	-1.07514×10^2	-9.21375×10^1	-6.83178×10^1	-1.07358×10^2	-9.21156×10^1	-4.22173×10^2	-1.11874×10^3	-5.16494×10^3
a_{i5}	1.42906×10^1	7.20344×10^1	1.25411×10^2	1.42891×10^1	7.20835×10^1	1.25484×10^2	5.23691×10^1	1.73098×10^2	7.85965×10^2
a_{i6}	-2.43583	-1.37501×10^1	-3.25984×10^1	-2.46506	-1.38060×10^1	-3.24417×10^1	-6.35869	-2.33743×10^1	-1.29447×10^2
a_{i7}	9.32623	-1.91793×10^1	-1.10903×10^2	9.35304	-1.91920×10^1	-1.10961×10^2	1.34509×10^2	3.60334×10^2	1.60224×10^3

Coefficients of the analytical function (equation (1)) of the $^{12}C+^{12}C$ reaction rate and of its upper and lower limits. They result from a fit of the numerical values given in Extended Data Table 2 using the reaction rate parameterizer from the NUCASTRODATA toolkit (http://www.nucastrodata.org/).

to determine the impact that the new $^{12}C + ^{12}C$ reaction rate will have in various astrophysical contexts.

1. Woosley, S. E., Heger, A. & Weaver, T. A. The evolution and explosion of massive stars. *Rev. Mod. Phys.* **74**, 1015–1071 (2002).
2. Keek, L. et al. First superburst from a classical low-mass X-ray binary transient. *Astron. Astrophys.* **479**, 177–188 (2008).
3. Cooper, R. L. et al. Possible resonances in the $^{12}C + ^{12}C$ fusion rate and superburst ignition. *Astrophys. J.* **702**, 660–671 (2009).
4. Iliadis, C. *Nuclear Physics of Stars*. (Wiley, Weinheim, 2007).
5. Caughlan, G. R. & Fowler, W. A. Thermonuclear reaction rates V. *At. Data Nucl. Data Tables* **40**, 283–334 (1988).
6. Spitaleri, C. et al. The Trojan Horse Method in nuclear astrophysics. *Phys. At. Nucl.* **74**, 1725–1739 (2011).
7. Tribble, R. et al. Indirect techniques in nuclear astrophysics: a review. *Rep. Prog. Phys.* **77**, 106901–106950 (2014).
8. Pignatari, M. et al. The $^{12}C + ^{12}C$ reaction and the impact on nucleosynthesis in massive stars. *Astrophys. J.* **762**, 31–54 (2013).
9. Abegg, R. & Davis, C. A. ^{12}Mg states observed via $^{20}Ne(\alpha,\alpha_0)^{20}Ne$. *Phys. Rev. C* **43**, 2523–2540 (1991).
10. Itoh, K. et al. Electroexcitation of giant multipole resonances in ^{24}Mg. *Phys. Rev. C* **23**, 945–959 (1981).
11. Yang, G. C. et al. Isoscalar multipole strength in ^{24}Mg through inelastic α scattering. *Phys. Rev. C* **13**, 1376–1387 (1976).
12. Vanhoy, J. R. et al. Proton resonances in ^{24}Mg from $E_x = 12.7$ to 15.7 MeV. *Phys. Rev. C* **36**, 920–932 (1987).
13. Bertrand, F. E. et al. Giant quadrupole resonance in $^{24,26}Mg$: a comparison of inelastic-scattering and α-capture experiments. *Phys. Rev. Lett.* **40**, 635–638 (1978).
14. Becker, H. W., Kettner, K. U., Rolfs, C. & Trautvetter, H. P. The $^{12}C + ^{12}C$ reaction at sub-Coulomb energies (II). *Z. Phys. A* **303**, 305–312 (1981).
15. Spillane, T. et al. $^{12}C + ^{12}C$ fusion reactions near the Gamow Energy. *Phys. Rev. Lett.* **98**, 122501–122505 (2007).
16. Lane, A. M. & Thomas, R. G. *R*-matrix theory of nuclear reactions. *Rev. Mod. Phys.* **30**, 257–353 (1958).
17. Aguilera, E. F. et al. New γ-ray measurements for $^{12}C + ^{12}C$ sub-Coulomb fusion: toward data unification. *Phys. Rev.* **73**, 064601–064612 (2006).
18. Mazarakis, M. G. & Stephens, W. E. Experimental measurements of the $^{12}C + ^{12}C$ nuclear reactions at low energies. *Phys. Rev. C* **7**, 1280–1287 (1973).
19. High, M. D. & Cujec, B. The $^{12}C + ^{12}C$ sub-Coulomb fusion cross section. *Nucl. Phys. A* **282**, 181–188 (1977).
20. Kettner, K. U., Lorenz-Wirzba, H. & Rolfs, C. The $^{12}C + ^{12}C$ reaction at subcoulomb energies. *Z. Phys. A* **298**, 65–75 (1980).
21. Barrón-Palos, L. et al. Absolute cross sections measurement for the $^{12}C + ^{12}C$ system at astrophysically relevant energies. *Nucl. Phys. A* **779**, 318–332 (2006).
22. Caciolli, A. et al. Proton elastic scattering and proton induced γ-ray emission cross-sections on ^{23}Na from 2 to 5 MeV. *Nucl. Instrum. Meth. Phys. Res. B* **266**, 1392–1396 (2008).
23. Zickefoose, J. $^{12}C + ^{12}C$ Fusion: Measurement and Advances Toward the Gamow Energy. PhD thesis, Univ. of Connecticut (2011); https://pqdtopen.proquest.com/doc/908637546.html?FMT=AI.
24. Jiang, C. L. et al. Reaction rate for carbon burning in massive stars. *Phys. Rev. C* **97**, 012801–012806 (2018).
25. Thielemann, F.-K., Arnould, M. & Truran, J. W. Thermonuclear reactions rate from statistical model calculations. In *Advances in Nuclear Astrophysics (2nd IAP Workshop)* (ed. Vangioni-Flam, E.) 525 (Les Editions Frontières, Gif sur Yvette, 1987).
26. Schatz, H. et al. Strong neutrino cooling by cycles of electron capture and β decay in neutron star crust. *Nature* **505**, 62–65 (2014).
27. Bravo, E. et al. Type Ia supernovae and the $^{12}C + ^{12}C$ reaction rate. *Astron. Astrophys.* **535**, A114 (2011).
28. Straniero, O., Piersanti, L. & Cristallo, S. Do we really know Mup (i.e. the transition mass between type Ia and core-collapse supernova progenitors)? *J. Phys. Conf. Ser.* **665**, 012008 (2016).

Author contributions A.T. and C.S. proposed the experiment. A.T., C.S., M.L.C., G.L.G., I.I., L.L., R.G.P., S.M.R.P., R.S. and G.G.R. set up and ran the experiment, which lasted about one month. S.C., M.G., S.H., H.P., M.L.S., S.R. and L.T. participated in the data collection. A.T. performed the data reduction and analysis. M.L.C. developed the modified *R*-matrix code for the one-level many-channel case. A.T. and M.L.C. performed the statistical analysis. A.T. performed *R*-matrix calculations, interpreted the results, prepared the figures and wrote the manuscript. C.S. and M.L.C. contributed on the interpretation of the results. M.L.C. assisted with the figure preparation. L.L., R.G.P. and R.S. assisted with the astrophysical interpretation. A.T., C.S., M.L.C., S.C., G.L.G., I.I., L.L., R.G.P., G.G.R., R.S., S.R. and L.T. revised the manuscript.

METHODS

THM basic features. The THM is an indirect technique aiming at measuring low-energy nuclear reactions unhindered by the Coulomb barrier and free of electron screening[6,7,29]. It has been used to study several reactions related to fundamental astrophysical problems[30–34]. In the THM, the low-energy cross-section of an A(x,b)B reaction is determined by selecting the quasi-free contribution of a suitable A(a,bB)s reaction that is measured. In quasi-free kinematics, particle a, chosen for its xs cluster structure, is used to transfer the participant cluster x to induce the reaction with A, while the other constituent cluster s remains a spectator to the A(x,b)B sub-process[6]. Because the transferred nucleus x is virtual, its energy and momentum are not linked by the usual energy–momentum relation for a free particle. This gives the A(x,b)B reaction its half-off-the-energy-shell (HOES) character. The quasi-free A(a,bB)s reaction can be sketched using a pole diagram (see Extended Data Fig. 2) with two vertices referring to a break-up (upper vertex) and to the A(x,b)B process (lower vertex). The A + a relative motion takes place at an energy above the Coulomb barrier, ensuring that the transfer of particle x occurs inside the nuclear field of A without undergoing Coulomb suppression or electron screening. However, the A + x reaction takes place at the sub-Coulomb relative energy E_{cm} because the excess of energy in the A + a relative motion is needed for the break-up of the Trojan Horse nucleus a = (xs). From the principles of energy and momentum conservation, we obtain:

$$E_{cm} = \frac{m_x}{m_x + m_A} E_A - \frac{p_s^2}{2\mu_{sF}} + \frac{\boldsymbol{p}_s \cdot \boldsymbol{p}_A}{m_x + m_A} - B_{xs} \quad (1)$$

with m_i and $\boldsymbol{p}_i$ the mass and momentum of particle i, $\mu_{ij} = m_i m_j/(m_i + m_j)$ the reduced mass of particles i and j, F the compound system (F = A + x = b + B) and $B_{xs} = m_s + m_x - m_a$ the binding energy of clusters x and s inside a. E_{cm} can vary within a range determined by the momentum of the spectator particle, $\boldsymbol{p}_s$, or its emission angle. As for $\boldsymbol{p}_s$, its values should not exceed the theoretical upper limit for the relative momentum p_{xs} between x and s (in the laboratory system, $\boldsymbol{p}_{xs} = \boldsymbol{p}_x = -\boldsymbol{p}_s$) represented by the on-the-energy-shell bound state wave number $\kappa_{xs} = (2\mu_{xs}B_{xs})^{1/2}$. This is the condition for the quasi-free mechanism to be dominant, for example, for the HOES cross-section to approach the on-energy-shell cross-section minimizing distortions. For the ^{14}N = (^{12}Cd) system, $\kappa_{xs} = 181$ MeV c^{-1} (where c is the velocity of light), exceeding by far the experimental p_s upper limit of about 80 MeV c^{-1}, which is fixed by the phase space populated in the present experiment. In the plane-wave impulse approximation, the three-body cross-section can be factorized into two terms corresponding to the vertices of Extended Data Fig. 1 and given by:

$$\frac{d^3\sigma}{d\Omega_B d\Omega_b dE_B} \propto KF \, |\Phi(p_{xs})|^2 \left[\frac{d^2\sigma_{xA \to bB}}{dE_{xA}d\Omega} \right]^{HOES} \quad (2)$$

where KF is a kinematical factor containing the final state phase space factor and it is a function of the masses, momenta and angles of the outgoing particles[6]; $|\Phi(p_{xs})|^2$ is the squared Fourier transform of the radial wave function for the $\chi(r_{xs})$ inter-cluster motion whose functional dependence is fixed by the xs system properties; $\left[\frac{d^2\sigma_{xA \to bB}}{dE_{xA}d\Omega} \right]^{HOES}$ is the HOES cross-section of the binary reaction.

One-level many-channel THM formalism. In the case of a multi-resonance A(x,b)B reaction, the so-called modified R-matrix approach has been developed[35,36] to account for its HOES nature in the extraction of the reduced widths γ from the THM reaction yield. Because the transferred particle does not obey the mass–shell equation, no entrance-channel penetration factor is present, making it possible to reach astrophysical energies with no need of extrapolation. Yet the same reduced widths appear in the THM and in the on-energy-shell cross-sections, so the ones extracted from THM data can be used to determine the direct $S(E)$ factor, without HOES effects. For isolated non-interfering resonances, the one-level many-channel formula can be used, so that the THM A(x,b)B cross-section in the plane-wave impulse approximation[35,37] takes the form:

$$\frac{d^2\sigma_{xA \to c'}}{dE_{xA}d\Omega_s} = NF \sum_i (2J_i + 1) \left| \sqrt{\frac{k_{c'}}{\mu_{c'}}} \frac{\sqrt{2P_{c'}} M_i(p_{xA} R_{xA}) \gamma_{xA}^i \gamma_{c'}^i}{D_i(E_{xA})} \right|^2 \quad (3)$$

with NF a normalization factor; $k_{c'}$ and $P_{c'}$ are the exit-channel wave number and penetration factor (c' runs over all exit channels), E_{xA} and R_{xA} are the x-A entrance-channel relative energy and channel radius[17] is set to 7.25 fm:

$$M_i(p_{xA} R_{xA}) = \left[(B_{xA} - 1) j_{l_i}(\rho) - \rho \frac{\partial j_{l_i}(\rho)}{\partial \rho} \right]_{\rho = p_{xA} R_{xA}} \quad (4)$$

where $j_{l_i}(\rho)$ is the spherical Bessel function for the l_i wave, $p_{xA} = \sqrt{2\mu_{xA}(E_{xA} + B_{xs})}/\hbar$, B_{xA} is an arbitrary boundary condition chosen to reproduce the observable resonance parameters[38,39] and $D_i(E_{xA})$ is the R-matrix denominator of one-level multi-channel formulas[15]:

$$D_i(E_{xA}) = E_i - E_{xA} - \sum_c (\gamma_c^i)^2 (S_c - B_c) - I \sum_c 2P_c (\gamma_c^i)^2 \quad (5)$$

with the sum running over all the open channels c; S_c and B_c are the shift function and the boundary condition for channel c and γ_c^i is the reduced width for the ith resonance and c channel, which enters the calculation of the on-energy-shell $S(E)$ factor free of electron screening and is not affected by the experimental energy resolution.

Experimental setup and channel selection. A ^{14}N beam at 30 MeV was delivered onto a carbon target, 100 μg cm^{-2} thick, with a spot size of 1 mm. The silicon telescopes were made up of a 38-μm ΔE-detector and a 1,000-μm position-sensitive E-detector (with intrinsic α resolution quoted as 0.3 mm for the position and about 0.5% for the energy) to measure the residual energy. They were placed symmetrically at either side of the beam direction, each covering laboratory angles 8° to 30°, and devoted to the detection of α-and-d and p-and-d coincidences. Angular conditions were selected to maximize the expected quasi-free contribution, fulfilling the requirement for the spectator particle d to retain its initial energy inside ^{14}N. Channel selection was accomplished by gating on the ΔE–E two-dimensional plots to select coincident d and α(p) loci. A typical ΔE–E spectrum is shown in Extended Data Fig. 3, where p, d and α loci are clearly visible. Kinematics were reconstructed under the assumption of either a ^{20}Ne (for the α + d channel) or a ^{23}Na (for the p + d channel) as an undetected particle. The Q-value variable was reported as a function of a kinematic variable, such as the energy or the angle of any one of the particles involved. In this representation, coincidence events of interest should lie on a horizontal line that cuts the Q-value axis at the expected value, because the Q-value depends only on the masses of the particles involved. A typical spectrum for the present experiment is shown in Extended Data Fig. 4 for the ^{12}C(^{14}N,α^{20}Ne)^{2}H reaction, where the Q-value is reported as a function of the α detection angle. Two dominant sharp horizontal loci appear, corresponding to the ground and first excited states of ^{20}Ne. They are highlighted by blue and red solid lines crossing the Q-value axis at −5.65 MeV and −7.28 MeV, respectively. This spectrum makes us confident of the quality of the calibration and of the correct selection of the reaction channel. Further data analysis was restricted to such events.

Deuteron momentum distribution. The d momentum distribution is a physical quantity very sensitive to the reaction mechanism. It keeps the same shape as inside ^{14}N only if the latter experiences quasi-free break-up. The agreement between the shapes of the theoretical and experimental momentum distributions is thus a compelling signature of occurrence of the quasi-free mechanism[6,7]. To determine the d momentum distribution from the coincidence yield, the modulation due to possible contributions of ^{24}Mg states has to be removed. This is done over restricted ranges of E_{cm} and θ_{cm} of less than 30 keV and 5°, respectively. The kinematic factor KF, describing the phase space population, is divided out by performing a Monte Carlo simulation of the experimental setup with the angular ranges and detection thresholds of the experiment. The momentum distribution from the ^{12}C(^{14}N,α$_0$^{20}Ne)^{2}H reaction is shown as an example in Extended Data Fig. 1 as black filled circles. Data are projected in 8 MeV c^{-1} bins over the momentum axis of the detected deuteron, p_d, with error bars including statistical errors only. The solid black line in the figure represents the theoretical behaviour normalized to experimental data. It is obtained from the Woods–Saxon ^{12}C d bound state potential with standard geometrical parameters $r_0 = 1.25$ fm, $a = 0.65$ fm and $V_0 = 54.428$ MeV, adjusted to give the experimental ground state ^{12}C$_{gs}$ d binding energy in ^{14}N. A fair accordance ($\tilde{\chi}^2 = 0.2$) shows up, indicating that in the phase space region spanned in the present experiment the reaction mainly proceeds through a direct ^{12}C transfer. Thus, the plane-wave impulse approximation factorization of equation (2) can be relied on for the present investigation because no distortions are needed within experimental errors to describe the transfer process[37]. This result agrees with previous work[40,41] where a strong transfer component is found in similar kinematic conditions with d detected at forward angles. We remark that in the present experiment the d centre-of-mass angular range is about 11°–50° and the coincidence mode triggers event acquisition. In those papers[40,41], it was taken into account that the transferred ^{12}C can be found also in its first excited 2$^+$ state at 4.44 MeV. From angular distribution analysis using a general expression for resonance reactions[42], there is no evidence in our experimental data of a ^{12}C transfer in its first excited 2$^+$ state at 4.44 MeV. It turns out that only transfer of ^{12}C in its ground state is contributing. This result will be discussed in a future paper.

From the shape analysis of the momentum distribution, we could estimate the possible contribution of reaction mechanisms other than the quasi-free one to the extracted experimental yield. In particular, other contributing mechanisms, such as

'compound nucleus' or 'multistep transfer', are represented by an isotropic momentum distribution as a signature of loss of correlation in the deuteron momentum. Thus, a fit of the experimental shape of the momentum distribution was performed with a linear combination of the theoretical function for the quasi-free mechanism with a constant one, leaving coefficients as free parameters. The covariance matrix fit returns a contribution consistent with zero for the constant function within an uncertainty of 3% at a 2σ level, including correlations. This contribution to the overall uncertainty was neglected in the further extraction of cross-sections and reaction rates.

Modified R-matrix analysis. Level energies and J^π values were taken from the literature[8,10–12]. In particular, J^π assignments were checked to be in agreement for the most prominent peaks in the present experiment through angular distribution analysis. Because the widths of the ^{24}Mg states at the relevant excitation energies are smaller than their average spacing[8,43] (for example, at $E_{cm} \approx 1.5$ MeV, $\Gamma/D < 0.4$, with Γ and D the level widths and spacings, respectively.) and most importantly, owing to the smoothing effect of our experimental resolution, interference between them was not taken into account. Indeed, the energy resolution removes the problem of interference, making our result insensitive to it[44]. Thanks to the non-overlapping nature of the levels involved, integration of the $d^3\sigma/dE_{cm}d\Omega_d d\Omega_{cm}$ over the $\alpha(p)$ emission angle in the centre-of-mass system of the ^{12}C(^{12}C,$\alpha_{0,1}$)^{20}Ne and ^{12}C(^{12}C,$p_{0,1}$)^{23}N sub-reactions could be easily performed. Because the experimental θ_{cm} range of the sub-reactions is about 140° to 180°, angular distributions outside this angular region were calculated by means of the general expression for resonance reactions[42]. If one considers the α_1 and p_1 fractions of the total fusion yield observed[13,14] at $E_{cm} > 2.8$ MeV, the lower limits of the $\alpha_0 + \alpha_1$ and $p_0 + p_1$ contributions to the total cross-sections from the present experiment at the highest energies are 0.85 ± 0.07 and 0.68 ± 0.06, respectively. However, the number of accessible excited states for both ^{20}Ne and ^{23}Na already reduces to half while moving from $E_{cm} = 2.8$ MeV to 1.5 MeV and the cross-sections for ^{20}Ne and ^{23}Na excited states drop more steeply than those for ground states, owing to the sharper decrease (by orders of magnitude) of the corresponding penetration factors. Monitoring the decrease of the penetration factors for the relevant states, and according to the results[13] at $E_{cm} < 3$ MeV, the contribution to the total fusion yield from α and p channels other than $\alpha_{0,1}$ and $p_{0,1}$ was neglected in the modified R-matrix analysis within uncertainties at $E_{cm} < 2$ MeV lower than 1% and 2% for the α and p channels, respectively.

For all of the states involved in the procedure, the total widths are known and in several cases one of the partial widths (usually the α_0 partial width). Thus, the normalization constant NF in equation (3) and the missing partial widths were the only free parameters to match the modified R-matrix calculations with the indirect data for the four channels. Each calculated cross-section was folded with a Gaussian function having $\sigma = 30$ keV to account for energy resolution, as calculated from the beam spot size and divergence, the position-sensitive E-detector intrinsic energy and angle resolution, energy and angular straggling in target and dead layers. Total and partial widths and related uncertainties resulting from the fit are listed in Extended Data Table 2 for all levels entering the calculation. Odd J assignments are uncertain by ± 1. Uncertainties account for the error budget affecting experimental data (statistical and from background subtraction, when applicable) and correlation among the resonances in the four reaction channels and range from 10% to about 20%.

Astrophysical $S(E)$ factor. This factor is introduced to remove the dominant energy dependence of the cross-section between charged particles at astrophysical energies that is due to Coulomb barrier penetration. The $S(E)$ factor (in units of MeV b) is defined through the relationship:

$$S(E) = E\sigma(E) exp(2\pi\eta) \tag{6}$$

where E is the incident energy in the centre-of-mass system, $\sigma(E)$ is the energy-dependent cross-section and $exp(2\pi\eta)$ is the inverse of the Gamow factor, with η the Sommerfeld parameter, $\eta(E) = Z_1 Z_2 \alpha(\mu c^2/2E)^{1/2}$ (where Z_1, Z_2 are the charges of the colliding nuclei, α is the fine structure constant, μ is the reduced mass in atomic mass units and c is the velocity of light).

For s-wave non-resonant reactions, the $S(E)$ factor is nearly independent of energy and it is the conventional quantity used to extrapolate to low energies.

For the ^{12}C + ^{12}C reaction, it is customary to use the so-called modified $S(E)$ factor, $S(E)^*$, which displays resonances more clearly. It is defined as:

$$S(E)^* = E\sigma(E) \times \exp(87.12E^{-1/2} + 0.46E) \tag{7}$$

where the exponential term is the inverse of the Gamow factor with a correction arising from the second term in the Coulomb barrier approximation[45]. In particular, the numerical factor 0.46 is the value of the size factor $g = 1/3(M_1M_2/(M_1 + M_2)R^3/2Z_1Z_2)^{1/2}$, with R_0 the nuclear separation and M_1, M_2 the masses of the colliding nuclei.

Numerical values of ^{12}C + ^{12}C reaction rate. Since the total ^{12}C + ^{12}C fusion yield at $E_{cm} < 2.8$ MeV is likely to be exhausted by the $\alpha_{0,1}$ and $p_{0,1}$ channels (see Methods section 'Numerical values of the ^{12}C + ^{12}C reaction rate'), we assume that the sum of their reaction rates in the E_{cm} range investigated here is representative of the total one. The numerical values of the total ^{12}C + ^{12}C reaction rate are given in Extended Data Table 2 expressed in units of cm^3 mol^{-1} s^{-1} at temperatures of $T = 0.1$–3 GK. The lower and upper limits are computed using the total uncertainty derived by combining the rate uncertainties in quadrature for the four channels investigated. Each channel propagates the uncertainty in the THM $S(E)^*$ factor. The last column of Extended Data Table 2 shows the exponents of the power of ten factor multiplying the three previous columns.

Data availability. All relevant data are available from the corresponding author on reasonable request. Data to calculate the rate ratio in Fig. 3 are included in Extended Data Table 2.

Code availability. We have not made publicly available the code for the modified R-matrix calculation because it is not intended for open use. However, it is available from the corresponding author upon request.

29. Strieder, F., Rolfs, C., Spitaleri, C. & Corvisiero, P. Electron-screening effects on fusion reactions. *Naturwissenschaften* **88**, 461–467 (2001).
30. Spitaleri, C. et al. Indirect ^{7}Li(p,α)^{4}He reaction at astrophysical energies. *Phys. Rev. C* **60**, 055802–055809 (1999).
31. Lamia, L. et al. An updated ^{6}Li(p,α)^{3}He reaction rate at astrophysical energies with the Trojan horse method. *Astrophys. J.* **768**, 65–73 (2013).
32. Tumino, A. et al. New determination of the ^{2}H(d,p)^{3}H and ^{2}H(d,n)^{3}He reaction rates at astrophysical energies. *Astrophys. J.* **785**, 96–113 (2014).
33. Pizzone, R. G. et al. First measurement of the ^{19}F(α,p)^{22}Ne reaction at energies of astrophysical relevance. *Astrophys. J.* **836**, 57–63 (2017).
34. Spitaleri, C. et al. Measurement of the ^{10}B(p,α)^{7}Be cross section from 5 keV to 1.5 MeV in a single experiment using the Trojan horse method. *Phys. Rev. C* **95**, 035801–035814 (2017).
35. Mukhamedzhanov, A. M. et al. Trojan Horse as an indirect technique in nuclear astrophysics. Resonance reactions. *J. Phys. G* **35**, 014016–014022 (2008).
36. La Cognata, M. et al. On the measurement of the ^{13}C(α,n)^{16}O S-factor at negative energies and its influence on the s-process. *Astrophys. J.* **777**, 143–164 (2013).
37. La Cognata, M. et al. Effect of high-energy resonances on the ^{18}O(p, α)^{15}N reaction rate at AGB and post-AGB relevant temperatures. *Astrophys. J.* **723**, 1512–1522 (2010).
38. Mukhamedzhanov, A. M. et al. Theory of deuteron stripping. From surface integrals to generalized R-matrix approach. *Phys. Rev. C* **84**, 044616–044622 (2011).
39. La Cognata, M. et al. The fluorine destruction in stars: first experimental study of the ^{19}F(p,α_0)^{16}O reaction at astrophysical energies. *Astrophys. J.* **739**, L54–L60 (2011).
40. Zurmühle, R. W. et al. Observation of ^{12}C cluster transfer by angular correlation measurements. *Phys. Rev. C* **49**, 2549–2554 (1994).
41. Belyaeva, T. L., Zelenskaya, N. S. & Aguero Granados, M. Investigation of quasimolecular states in ^{24}Mg*Mg through the analysis of the angular dα correlations in the ^{12}C(^{14}N,d)^{24}Mg(α)^{20}Ne reaction. *Phys. At. Nucl.* **65**, 1616–1627 (2002).
42. Blatt, J. M. & Biedenharn, L. C. The angular distribution of scattering and reaction cross sections. *Rev. Mod. Phys.* **24**, 258–272 (1952).
43. Jiang, C. L. et al. Origin and consequences of ^{12}C + ^{12}C fusion resonances at deep sub-barrier energies. *Phys. Rev. Lett.* **110**, 072701–072705 (2013).
44. La Cognata, M. et al. A Trojan Horse approach to the production of ^{18}F in novae. *Astrophys. J.* **846**, 65–71 (2017).
45. Patterson, J. R., Winkler, H. & Zaidins, C. S. Experimental investigation of the stellar nuclear reaction ^{12}C + ^{12}C at low energies. *Astrophys. J.* **157**, 367–373 (1969).
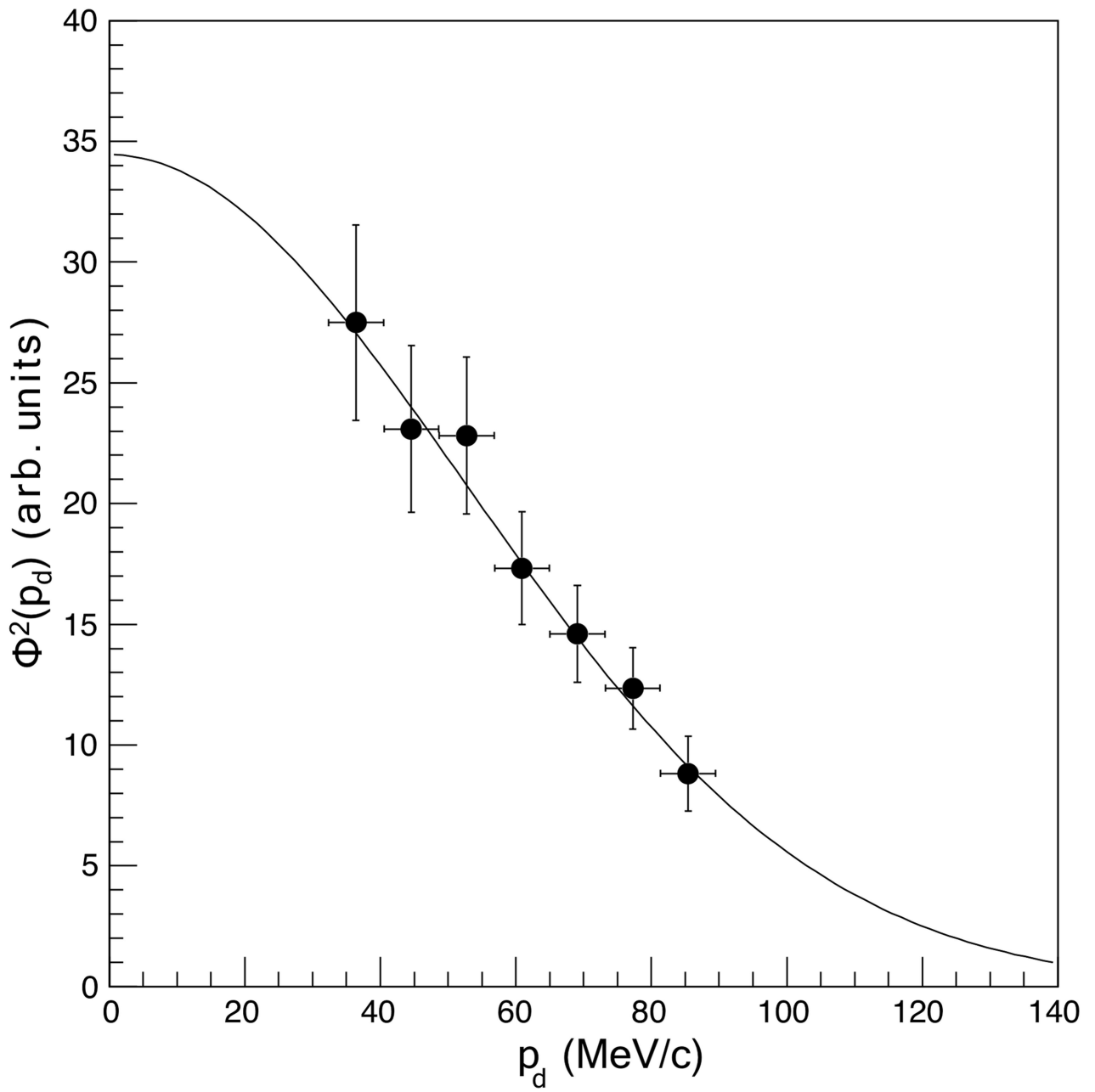
Extended Data Fig. 1 | Deuteron momentum distribution. The experimental distribution $\Phi^2(p_d)$ is shown as filled black circles. Error bars represent standard 1σ uncertainties. The black line represents the theoretical shape (see text for details).
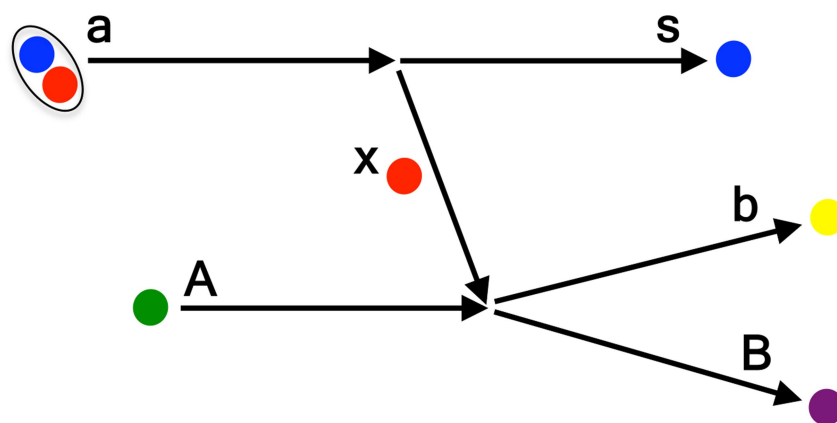
Extended Data Fig. 2 | Pole diagram describing the quasi-free mechanism in the A(a,bB)s reaction. The upper vertex refers to the break-up of a and the lower vertex shows the A(x,b)B process. Colours help to highlight the role of individual particles in the mechanism.
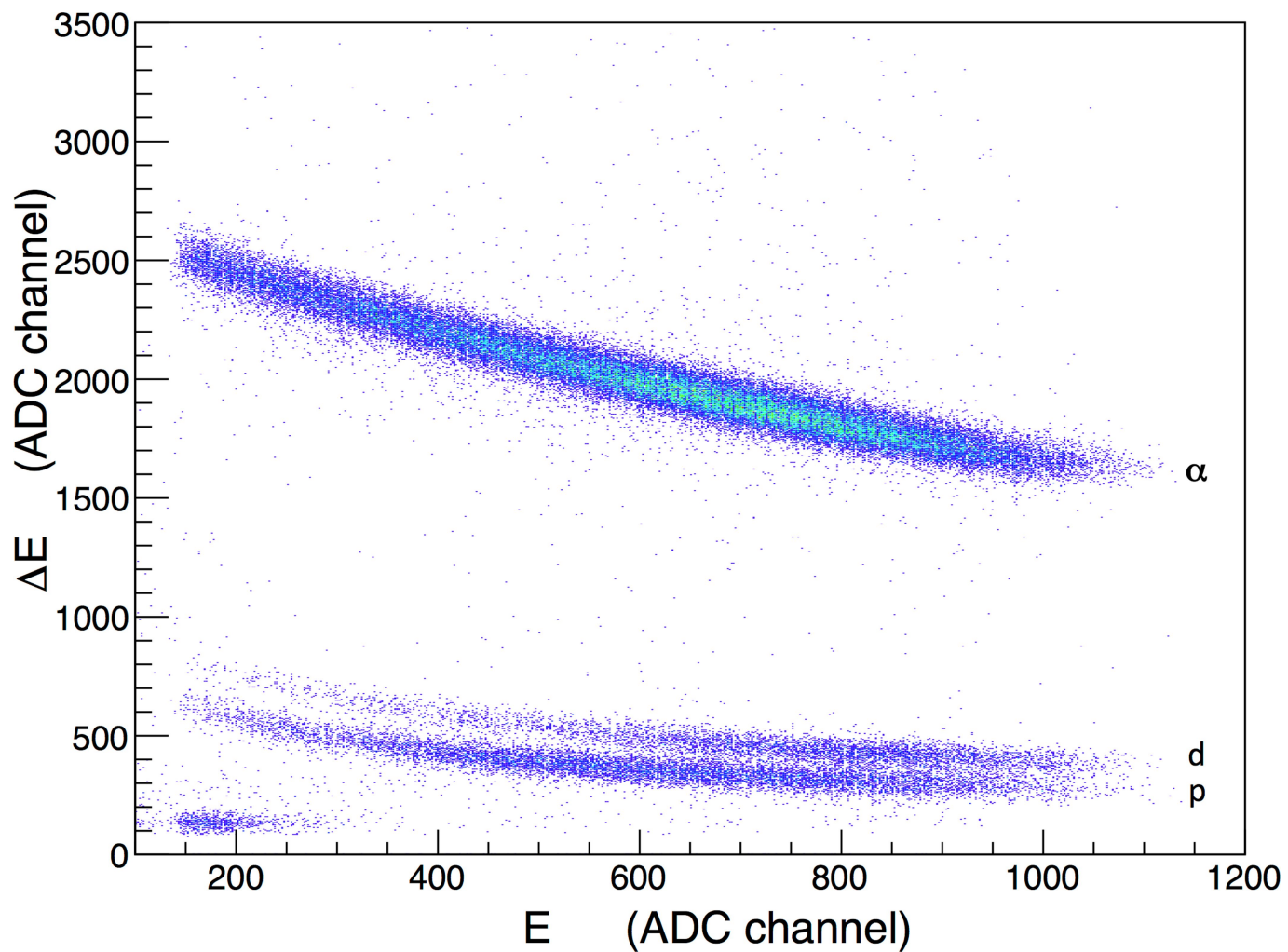
Extended Data Fig. 3 | Typical Δ*E*–*E* spectrum. The strongest loci from the bottom to the top correspond to *p*, d and α. ADC, analogue-to-digital converter.
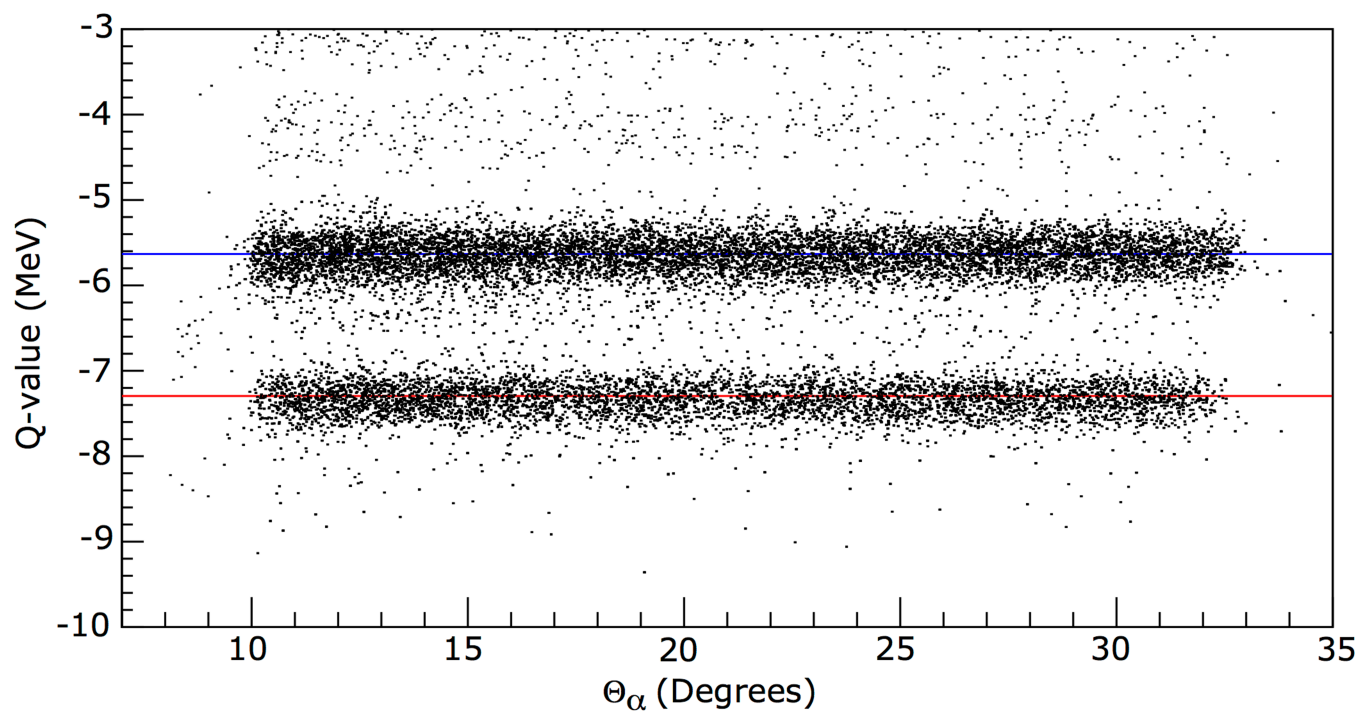
Extended Data Fig. 4 | Q-value as a function of the α detection angle Θ_α for the $^{12}C(^{14}N,\alpha^{20}Ne)^2H$ reaction. Blue and red solid lines cross the Q-value axis at -5.65 MeV and -7.28 MeV, highlighting the contributions of the ground and first excited states, respectively.

Extended Data Table 1 | Resonance parameters of ^{24}Mg levels entering the *R*-matrix fit and total plus partial widths resulting from the fit

$E_{c.m.}$ (MeV)	E_x (MeV)	J^π	$\Gamma_{c.m.}$ (keV)	$\Gamma_{\alpha 0}$ (keV)	$\Gamma_{\alpha 1}$ (keV)	Γ_{p0} (keV)	Γ_{p1} (keV)
2.664	16.597	4^+	29.3±6.1	10.7±2.2	16.6±3.5	1.1±0.2	0.90±0.18
2.567	16.500	0^+	42.8±4.8	4.8±0.9	36.5±3.7	0.7±0.1	0.8±0.1
2.537	16.470	6^+	6.91±0.95	2.0±0.4	3.9±0.4	0.7±0.1	0.31±0.05
2.5	16.433	7^-	9.6±1.1	0.9±0.2	8.6±0.9	0.07±0.01	0.019±0.003
2.455	16.388	2^+	37.5±5.4	15.1±2.7	18.0±1.9	4.1±0.8	0.31±0.04
2.403	16.336	4^+	22.4±2.8	4.6±0.8	15.4±1.6	1.7±0.3	0.7±0.1
2.369	16.302	8^+	0.49±0.07	0.18±0.03	0.22±0.02	0.06±0.01	0.032±0.005
2.338	16.271	4^+	37.9±5.6	13.6±2.5	16.2±1.7	4.6±0.9	3.5±0.5
2.263	16.196	6^+	7.3±1.2	3.3±0.6	2.2±0.2	1.3±0.3	0.45±0.07
2.196	16.129	3^-	31.6±4.3	1.0±0.2	18.8±1.9	8.8±1.7	3.0±0.5
2.095	16.03	2^+	7.2±1.1	1.1±0.3	1.7±0.4	3.4±0.4	1.00±0.02
2.038	15.971	5^-	43.9±4.4	15.2±2.0	26.5±1.8	2.1±0.5	0.10±0.02
1.946	15.879	4^+	43.4±7.6	4.0±0.7	8.4±0.9	27.4±5.5	3.6±0.5
1.888	15.821	3^-	87±16	5.3±0.9	8.0±0.9	65±13	8.1±1.3
1.853	15.786	4^+	12.8±1.9	2.4±0.4	5.2±0.5	3.8±0.8	1.3±0.2
1.777	15.71	4^+	30.6±4.6	9.0±1.6	13.1±1.3	8.0±1.6	0.45±0.07
1.747	15.68	0^+	4.8±0.6	0.38±0.07	3.3±0.3	1.0±0.2	0.10±0.02
1.671	15.604	2^+	29.0±4.2	6.3±1.1	13.1±1.3	7.7±1.5	1.9±0.3
1.593	15.526	6^+	23.7±3.3	8.3±1.5	13.7±1.4	1.3±0.3	0.40±0.06
1.544	15.477	2^+	17.1±2.1	1.0±0.2	12.5±1.2	3.5±0.7	0.07±0.01
1.503	15.436	2^+	12.6±1.9	1.7±0.3	5.7±0.6	4.6±0.9	0.7±0.1
1.445	15.378	4^+	31.9±4.7	10.4±1.9	14.0±1.4	5.2±1.1	2.2±0.3
1.414	15.347	4^+	16.6±2.5	8.0±1.4	6.2±0.6	2.3±0.5	0.10±0.01
1.37	15.31	5^-	9.1±1.5	0.07±0.01	3.5±0.4	5.5±1.1	0.02±0.003
1.293	15.226	4^+	25.1±4.2	0.6±0.1	7.6±0.8	16.0±3.2	0.9±0.1
1.274	15.207	5^-	39.3±6.4	26.9±4.9	9.2±0.9	2.7±0.5	0.6±0.08
1.239	15.172	4^+	60.8±9.3	28.1±5.1	20.6±2.1	5.1±1.0	7.0±1.1
1.201	15.134	4^+	15.7±1.8	0.49±0.09	12.9±1.3	2.0±0.4	0.30±0.04
1.175	15.108	4^+	16.6±2.5	1.6±0.3	6.7±0.7	5.6±1.1	2.8±0.4
1.055	14.988	5^-	10.4±1.8	0.5±0.1	3.1±0.3	6.0±1.1	0.8±0.3
0.988	14.921	0^+	12.9±1.8	2.1±0.5	7.9±0.7	2.5±0.6	0.40±0.03
0.909	14.842	2^+	14.9±1.8	2.1±0.4	3.6±0.3	7.8±0.9	1.4±0.2
0.877	14.81	1^-	5.6±0.6	2.1±0.2	0.40±0.08	3.0±0.3	0.10±0.02
0.805	14.738	4^+	8.6±1.3	2.2±0.3	0.11±0.02	2.7±0.6	3.6±0.4

Quoted uncertainties are ±1σ. Parameters are the centre-of-mass energy E_{cm}, the excitation energy E_x, the spin and parity J^π, the total width Γ_{cm}, the α_0 partial width $\Gamma_{\alpha 0}$, the α_1 partial width $\Gamma_{\alpha 1}$, the p_0 partial width Γ_{p0} and the p_1 partial width Γ_{p1}.

Extended Data Table 2 | Reaction rate of the $^{12}C + ^{12}C$ fusion reaction

| | Reaction Rate $(cm^3 s^{-1} mol^{-1})$ | | | |
T (GK)	Adopted	Lower	Upper	Power
0.10	2.77	2.77	2.77	-52
0.11	7.80	7.69	7.91	-50
0.12	1.71	1.52	1.89	-47
0.13	4.59	3.55	5.64	-45
0.14	0.90	0.66	1.14	-42
0.15	0.97	0.71	1.24	-40
0.16	6.00	4.33	7.66	-39
0.18	5.85	4.21	7.49	-36
0.20	1.46	1.05	1.86	-33
0.25	3.12	2.25	3.99	-29
0.30	2.62	1.89	3.36	-26
0.35	3.91	2.82	5.01	-24
0.40	3.05	2.19	3.90	-22
0.45	1.95	1.40	2.49	-20
0.50	7.65	5.51	9.80	-19
0.60	2.49	1.79	3.19	-16
0.70	1.90	1.37	2.44	-14
0.80	5.97	4.30	7.63	-13
0.90	1.05	0.76	1.34	-11
1.00	1.24	0.91	1.56	-10
1.25	1.88	1.53	2.22	-08
1.50	1.03	0.93	1.11	-06
1.75	2.79	2.69	2.89	-05
2.00	4.41	4.35	4.47	-04
2.50	3.34	3.33	3.35	-02
3.00	0.86	0.86	0.86	00

The recommended value, 1σ lower and upper limits were computed at $T = 0.1$–3 GK covering the relevant astrophysical region. In the last column, the exponents of the power of ten multiplying columns 2, 3 and 4 are given.